JOURNAL OF AIRCRAFT
Vol. 46, No. 1, January–February 2009

Transport Aircraft Wake Influenced by Oscillating Winglet Flaps

Christian Breitsamter* and Alexander Allen†
Technische Universität München, 85747 Garching, Germany

DOI: 10.2514/1.37307

The wake vortex development in the near field and extended near field behind a four engined large transport aircraft model fitted with an active winglet is presented. A detailed wind-tunnel investigation is conducted using a half-model focusing on the high-lift case of a typical approach configuration at a Reynolds number of 0.5×10^6 based on the wing mean aerodynamic chord and an angle of attack of 6.5 deg. The flowfield is observed using advanced hot-wire anemometry mainly focusing on the crossflow plane at 5.6 spans downstream of the model. Based on the time-dependent velocity components the wake flowfield is analyzed by distributions of mean vorticity, turbulence intensities, and spectral densities. Seven main vortical structures dominating the near-field wing vortex sheet roll up and merge to form the remaining trailing vortex in the extended near field. By the use of oscillating winglet flaps the velocity fluctuations at the core region of the remaining vortex are significantly influenced. Distinct narrowband concentrations of turbulent kinetic energy can be found for the farthest downstream plane documenting the presence of the disturbances generated by the winglet flaps which may result in an amplification of inherent far-field instabilities. The frequencies at which these narrowband energy concentrations occur are, on the one hand, dependent on the oscillation frequency of the winglet flaps; on the other hand, there are also independent energy concentrations within the frequency bands associated with wake instabilities.

Nomenclature

AR	=	aspect ratio
b	=	wing span, m
b_0	=	main vortex pair distance, m
$\tilde{b}_0$	=	distance between two adjacent vortices of a four vortex system, m
C_D	=	drag coefficient
C_L	=	lift coefficient, $2LAR/(\rho U_\infty^2 b^2)$
C_m	=	pitching moment coefficient
$\bar{c}$	=	wing mean aerodynamic chord, m
f	=	frequency, Hz
f_M	=	sampling frequency, Hz
k	=	reduced frequency, $fb/(2U_\infty)$
L	=	lift, N
n_B	=	number of band-averaging intervals
$Re_{\bar{c}}$	=	Reynolds number, $U_\infty \bar{c}/\nu$
r_c	=	vortex core radius, m
$S^N_{c,u'}$	=	cross-spectral density of u' normalized with $(\Delta k U_\infty)/(\overline{u'^2}(b/2))$
$S^N_{u'}$	=	power spectral density of u' normalized with $(\Delta k U_\infty)/(\overline{u'^2}(b/2))$
s	=	load factor, $\pi/4 = 0.7854$ for an elliptic lift distribution
Tu_x, Tu_y,	=	axial, lateral, vertical turbulence intensity, $\sqrt{\overline{u'^2}}/U_\infty$, $\sqrt{\overline{v'^2}}/U_\infty$
Tu_z	=	$\sqrt{\overline{w'^2}}/U_\infty$
U_∞	=	freestream velocity, m/s
u, v, w	=	axial, lateral, and vertical velocities, m/s
$\bar{u}$, $\bar{v}$, $\bar{w}$	=	mean axial, lateral, and vertical velocities, m/s
u', v', w'	=	fluctuation part of u, v, and w, m/s
w_0^*	=	downwash velocity with respect to Γ_0^*, m/s, $\Gamma_0^*/(2\pi b_0)$
x^*	=	nondimensional distance in x direction, x/b; $x^* = 0$ at winglet tip trailing edge for $\alpha = 0$ deg
y^*, z^*	=	nondimensional distances in y and z directions, $2y/b$, $2z/b$
α	=	aircraft angle of attack, deg
Γ_0^*	=	root circulation based on an elliptic circulation distribution, m^2/s $(C_L U_\infty b)/(2ARs)$
δ	=	winglet flap deflection, deg
λ	=	wavelength, m
ν	=	kinematic viscosity, m^2/s
ξ	=	nondimensional axial vorticity, $\bar{\omega}_x b/(2U_\infty)$
ρ	=	density, kg/m^3
τ^*	=	nondimensional time, $x^* 16 C_L/(\pi^4 \mathrm{AR})$
$\bar{\omega}_x$	=	mean axial vorticity component, $(\mathrm{d}\bar{w}/\mathrm{d}y - \mathrm{d}\bar{v}/\mathrm{d}z)$, 1/s

Subscripts

Crouch	=	Crouch instability
Crow	=	Crow instability
d	=	dominant
max, min	=	maximum, minimum
osc	=	oscillating

Received 26 February 2008; revision received 10 October 2008; accepted for publication 10 October 2008.

*Privatdozent, Dr.-Ing., Chief Scientist, Institute of Aerodynamics. Associate Fellow AIAA.

†Dipl.-Ing., Master of Science, Research Engineer, Institute of Aerodynamics. Member AIAA

Introduction

MAJOR airports around the world are encountering a long term capacity problem due to the growing difficulties in expanding airports and runways. Aircraft size is increased to compensate this development. As the minimum separation distance between two aircraft during approach, takeoff, and enroute is solely driven by the maximum takeoff weight and therewith by the size of the two involved aircraft [1,2], the compensation may well lead to a loss in passenger numbers per hour, if the separation distances of future large transport aircraft are increased beyond their increase in seating capacity in comparison to the aircraft operating today. The Federal Aviation Administration in the U.S. and the Civil Aviation Authority in Europe regulate the separation distances, which are estimated conservative to account for the varying behavior of the vortices under different atmospheric conditions [3]. The aim of numerous activities is to reduce aircraft separation distances to meet the requirements of

growing air traffic, without reducing the level of safety already obtained today and therewith relieve hub airports.

Wake vortical structures and related problems have been intensively investigated in the past [4–7]. The behavior of the trailing wake of a lifting body is well known. It rolls up into a pair of strong counter-rotating longitudinal vortices that persist for many body dimensions downstream. The vortex strength is proportional to the bound circulation or body lift, and hence, for steady flight conditions this is approximately proportional to the weight of the generating aircraft. An aircraft encountering a vortex wake can experience a rolling motion, if the following aircraft enters the wake of the preceding aircraft and by coincidence meets the vicinity of the vortex axis. Also a sudden upwash or downwash can occur, leading to increased structural loads or a dangerous change in climb rate, which is especially critical close to the ground. In any case a rapid change of attitude possibly combined with heavy disturbances of trimmed flight conditions can occur.

Wake vortex physics and means of wake vortex alleviation have been addressed in several integrated research projects [8–10]. Various experimental and numerical methods have been used to study the wake vortex evolution and development [11,12]. Tests have been and still are conducted on generic models as well as on detailed transport aircraft models in wind tunnels, towing tanks, and catapults in order to deliver complementary data resulting in a sound description of the structure of the wake vortices progressing downstream. Further, flight tests have been performed using triangular lidar measurements to observe and reveal the development of a wake generated by an aircraft under real meteorological conditions [13]. Additionally, computational methods, such as vortex filament methods, Reynolds-averaged Navier–Stokes computations, and large eddy simulations, are widely used to describe all stages of the wake vortex development [14–16]. The advanced numerical methods include also the influence of turbulence and unsteady effects on the wake vortex development. Experimental studies have demonstrated the importance of such effects [17].

Today's technology is not at the stage to track or predict wake vortex locations under all weather conditions. Therefore, many research activities concentrate on alleviating the wake vortex hazard by modifications of wing geometry and/or wing loading. Strategies to minimize the wake vortex hazard concentrate, on the one hand, on a low vorticity vortex design, which reduces the wake vortex hazard by enhancing the dispersion of the vorticity field. It is aimed on the generation of wake vortices with larger core size and smaller swirl velocities at the core radius after roll up is completed. Also, an optimum wing load distribution may minimize the induced rolling moment for a following aircraft [18]. The alteration of the circulation distribution of the wake generating wing can be obtained, for example, by using differential flap settings or spoiler settings. It has been shown that a wing with an outboard partially deflected flap and an inboard fully deflected flap produces, at least in the extended near field, a smaller induced rolling moment than a wing with a standard flap setting [19]. On the other hand, the focus is on a quickly decaying vortex [11]. An enhanced vortex decay may be achieved by promoting three-dimensional instabilities by means of passive or active devices [20–22]. Because a multiple vortex system shows instabilities which can grow more rapidly, passive devices aim to promote these kinds of instabilities through the deliberate production of single vortices in addition to those coming from the wing tip and the flap edge [11,20,23]. The production of additional distinct vortices can also be achieved by a differential flap setting. The efficiency of these concepts depends on the persistence of such additional vortex pairs which is determined by configurational details of the aircraft.

Especially, active devices are considered as a possible powerful mean to amplify wake vortex instabilities. In the mid 1970s, theoretical and experimental studies dealt with the influence of sinusoidally moving flaps on the wake vortex behavior and predicted a reduction in the wake life span by a factor of 3 [5,24]. In the last years, such means were carefully investigated again. An active system was proposed by Crouch et al. based on periodic oscillations of control surfaces, for example, ailerons and flaperons [25,26]. The perturbations influence the vortex wake to trigger inherent instabilities which, after sufficient amplification, may cause an earlier breakup of the trailing vortices into vortex rings resulting in a rapid decay. Further investigations concentrate on towing tank experiments using models of generic wing configurations. The oscillating devices include inner and outer ailerons [27], trailing-edge flaps [28,29], and winglet flaps [28]. In addition, unsteady Reynolds-averaged Navier–Stokes calculations have been carried out for a configuration with oscillating trailing-edge flaps [29]. Depending on the streamwise distance the wake vortex hazard is reduced up to a certain extent quantified, for example, by the maximum induced rolling moment or vorticity distribution. Other means, such as separation control by zero mass-flux blowing slots at flap edges [30] and active Gurney flaps [31] are also under consideration.

The results presented herein concentrate on the near-field wake characteristics of a large transport aircraft featuring a large winglet fitted with two trailing-edge flaps. The lower and upper winglet flaps can be deflected in the same direction (symmetrical case) or in the opposite direction (asymmetrical case). The influence of symmetric and asymmetric static flap deflections on the wake flowfield is discussed in [32] whereas here the influence of flap oscillations is addressed. The flowfield development is characterized by axial vorticity distributions, turbulence intensity patterns, and spectral densities. The investigation documents the wake vortex formation and analyzes the influence of the oscillating winglet flaps on the rolled-up trailing vortex characteristics. The focus is to demonstrate that the frequency dependent fluctuations generated in the near field (instabilities at $x^* = 0$) are present at the farthest downstream plane (at $x^* = 5.6$). Such disturbances are aimed at amplifying the development of inherent far-field wake instabilities.

Experimental Setup

The wind-tunnel facility C of the Institute of Aerodynamics at the Technische Universität München was used for this investigation employing a detailed large transport aircraft configuration and applying advanced hot-wire anemometry.

Wind Tunnel

The wind tunnel C is a closed-return type with a cross section of 1.8×2.7 m^2 and has a test section length of 21 m, which covers a wake distance of approximately 5.6 spans downstream of the model. The maximum usable velocity is 30 m/s. The turbulence level at the nozzle exit is less than 0.5%. The ceiling is adjustable to control the axial pressure gradient along the test section. With the model in place the axial pressure gradient is set close to zero to ensure unaffected wake development.

Model

Figure 1 illustrates the 1:32 scaled half-model of a typical large transport aircraft, which was used for this investigation. The model has a wing semispan ($b/2$) of 1.242 m (aspect ratio AR = 8.0, taper

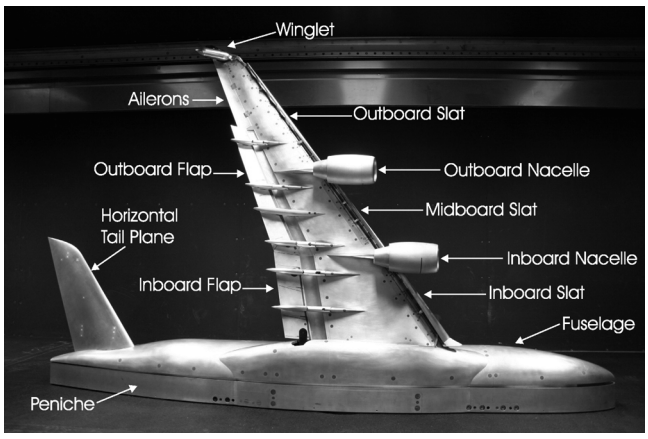

Fig. 1 Half-model of large transport aircraft installed in test section of wind tunnel C.

ratio 0.21), a wing mean aerodynamic chord of $\bar{c} = 0.362$ m, and a fuselage length of 2.119 m. The model is manufactured from aluminum and it is equipped with fully adjustable flaps, slats, ailerons, and horizontal tail plane and through-flow engine nacelles. To raise the model fuselage above the wind-tunnel floor boundary layer a peniche of 0.095 m height is used regarding typical low-speed conditions. The experiments concentrate on the approach configuration with a typical setting of the high-lift devices. The inboard and midboard slats are set to 26.5 deg, whereas the outboard one is deflected to 30.0 deg. The inboard and outboard flap are extended to 26.0 deg and the ailerons (inboard and outboard) are adjusted to 5 deg. Slat and flap positions and gaps are predefined for low-speed testing. To achieve a typical setting corresponding to straight and level flight, where the pitching moment is zero, the horizontal tail plane is set to -10.0 deg.

The wake flowfield is investigated for the configuration with a large winglet, which includes two trailing-edge flaps used to influence the wake vortex evolution. The winglet is especially manufactured for this investigation from titanium, Fig. 2. To supply sufficient space for the driving components of the flap actuator system the airfoil NACA65A012 is chosen. The winglet is equipped with a lower and upper movable trailing-edge flaps, the deflections of which are statically or dynamically up to $\delta = \pm 20$ deg. The flaps can be moved in phase, that is, in the same direction (symmetrical case), or with 180 deg phase shift (asymmetrical case), where the winglet flaps are deflected in opposite directions. The winglet is designed for oscillating frequencies up to $f = 100$ Hz; nevertheless only frequencies up to 40 Hz are investigated here. The rotational speed of an electronic servomotor controls the oscillation frequency. The housing of this motor is manufactured as a tilted cylinder at the wing tip lower side, Fig. 2, and has only a minor influence on the overall flowfield and wake vortex evolution [32].

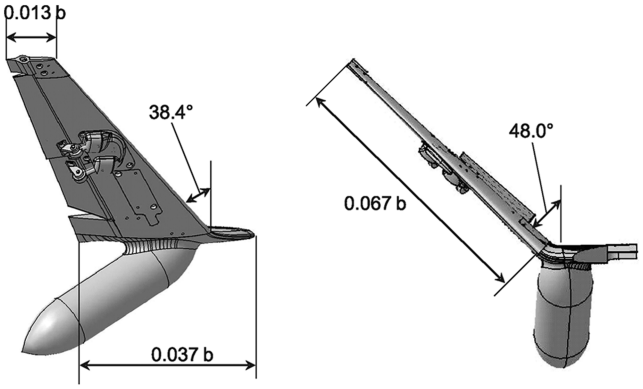

a)

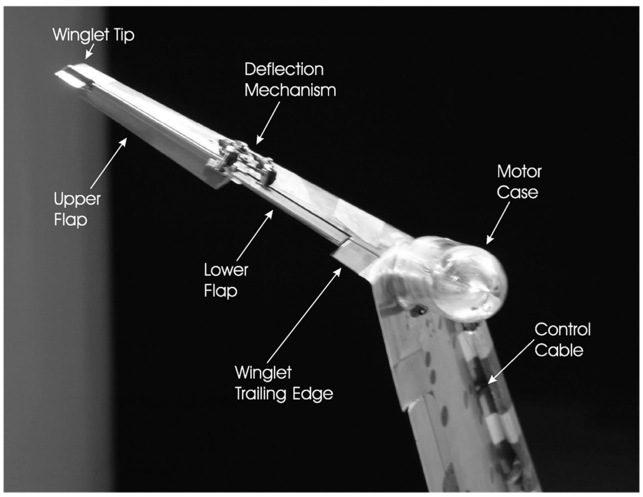

b)

Fig. 2 Large winglet with trailing-edge flaps: a) geometry; b) system elements.

Measurement System and Test Conditions

To obtain a time series of axial, lateral, and vertical velocities a triple-wire probe operated by a multichannel constant temperature anemometer system is used. The tungsten wires are platinum plated and have a diameter of 5 μm and a length of approximately 1.25 mm. To achieve the best angular resolution the wires are arranged perpendicular to each other. An additional temperature probe is employed to correct anemometer output voltages if ambient flow temperature varies. A sampling rate of 3000 Hz, a low pass filter frequency of 1000 Hz, and a sampling time of 6.4 s are chosen. Considering an exact digital reconstruction of the hot-wire voltage time series, that is, avoiding any aliasing effect, the usable frequency content is limited by the Nyquist frequency which is half the sampling rate (here, 1500 Hz). Therefore, the analog low pass filter is set to a value lower than the Nyquist frequency to eliminate the frequency content which cannot be captured by the digital reconstruction. The sampling time corresponds to 19,200 values per wire and survey point. The signals are digitized with 16 bit precision through a 16 channel simultaneous sampling A/D converter. To ensure that all relevant flowfield phenomena are detected, the sampling parameters are determined by preliminary tests. A look-up table is obtained from a full velocity (0–35 m/s) and flow angle (± 35 deg) dependent calibration of the hot-wire probe conducted before the flowfield measurements. The chosen calibration range captures all values occurring during the flowfield surveys. The numerically refined look-up table is then used to convert the anemometer output signals into time-dependent axial, lateral, and vertical velocity components u, v, and w. The corresponding methods are described in [33]. Based on statistical error evaluation, accuracies are in the range of 1% for mean quantities, 2.5% for rms quantities (turbulence intensities), and 4% for spectral densities [17,33].

The investigations are all performed at a freestream velocity of $U_\infty = 25$ m/s corresponding to a Reynolds number of $Re_{\bar{c}} = 0.5 \times 10^6$ based on the wing mean aerodynamic chord. The angle of attack is chosen to be $\alpha = 6.5$ deg with the corresponding lift coefficient being $C_L = 1.43$. The lift coefficient is determined by force measurements using an external six-component balance. Measurement accuracies related to the underfloor six-component wind-tunnel balance are 0.025% based on maximum loads of the balance load cells. Conducting half-model tests maximum allowable loads refer to 1500 N in the axial direction, ± 3000 N in the normal direction, and ± 700 Nm in the pitching moment. Thus, minimum detectable loads for axial force, normal force, and pitching moment are 0.38 N, 1.5 N, and 0.18 Nm, respectively. Thus, an accuracy in drag coefficient, lift coefficient, and pitching moment coefficient of $\Delta C_D = 0.0028$, $\Delta C_L = 0.011$, and $\Delta C_m = 0.0037$ is obtained for the present test. No transition strips are attached to the model as the inspection of the surface flow with tufts revealed attached flow on wing and horizontal tail plane.

The model is positioned on the wind-tunnel floor with the wing tip pointing upwards and the wing reference point (WRP) at 2.8 m downstream of the nozzle exit, Fig. 1. The WRP is the position of the winglet tip trailing edge at an angle of attack of $\alpha = 0.0$ deg, where $x^* = 0.0$. The model wing box is attached to the driven shaft of a computer controlled model support located below the test section floor, allowing a precise angle-of-attack setting. The test section is further equipped with a three axis probe traversing system giving minimum steps of ± 0.2 mm in the axial, lateral, and vertical directions. The vortex wake is measured in seven crossflow planes orientated perpendicular to the freestream direction at distances of $x^* = x/b = 0.02, 0.37, 1.0, 2.0, 3.0, 4.0$, and 5.6 downstream of the WRP. Here, the main focus is on the most downstream plane at station $x^* = 5.6$. In regions of high flow gradients, that is, in areas of vorticity layers and vortex cores, the survey points are closely spaced with a relative grid resolution of 0.004 in the spanwise and 0.006 in the vertical direction based on the wing span. Outside of these

regions the relative spacing is gradually enlarged to 0.024 laterally and 0.036 vertically. Regarding the susceptibility of vortical structures to intrusive measurements, it was found that the presence of the hot-wire probe has no markable influence on the wake vortex formation and evolution comparing flowfields obtained by probe and particle image velocimetry measurements [11].

Results and Discussion

A vortex wake can be divided into four main regions regarding the downstream development: 1) the near field, $x/\bar{c} \approx 1$, which is characterized by the formation of highly concentrated vortices shed at all surface discontinuities; 2) the extended near field, $x^* \leq 10$, where the wake roll-up process takes place, and the merging of dominant vortices (flap edge, wing tip) occurs, leading gradually to two counter-rotating vortices; 3) the far field, $10 \leq x^* \leq 100$, where the wake is descending in the atmosphere and linear instabilities emerge; and 4) the decay region, $x^* > 100$, where fully developed instabilities cause a strong interaction between the two trailing vortices until they collapse. The results shown here are solely for the near field and extended near field. The downstream stations are marked by the nondimensional distance x^* and the nondimensional characteristic time $\tau^* = x^* 16 C_L/(\pi^4 \mathrm{AR})$. The latter number includes lift coefficient and aspect ratio to compare results of different tests and configurations with reference to an elliptic lift distribution. The flowfields are presented as contour plots of nondimensional axial vorticity $\xi = \bar{\omega}_x b/(2U_\infty)$ and vertical turbulence intensity Tu_z. The term $\bar{\omega}_x$ indicates the mean axial vorticity component $(\mathrm{d}\bar{w}/\mathrm{d}y - \mathrm{d}\bar{v}/\mathrm{d}z)$.

Baseline Configuration

To quantify the overall development of the wake vortex flowfield, a detailed investigation is conducted using the large winglet without deflection or oscillation of the winglet flaps. The nondimensional axial vorticity distribution and turbulence intensities of the crossflow plane at $x^* = 0.37$, $\tau^* = 0.011$, are shown in Fig. 3. The main near-field vortices are marked by the corresponding acronyms and their peak vorticity levels are stated. Note that the vorticity levels $-1.0 < \xi < 1.0$ are blanked in all those figures, to clarify the positions of dominating vortices. Turbulence intensity levels of $Tu_z < 0.02$ are also blanked to emphasize the vortex sheet emanating from the wing more clearly.

Seven main vortices can be identified, namely, from outboard to inboard, the winglet vortex (WLV), the wing tip vortex (WTV), the outboard nacelle vortex (ONV), the outboard flap vortex (OFV), the inboard nacelle vortex (INV), the horizontal tail plane vortex (HTV) and the merged inboard flap vortex and wing-fuselage vortex (IFV/WFV), Fig. 3a. Negative vorticity is attributed to the HTV and the IFV/WFV; these vortices are therefore counter-rotating in comparison to the other five vortices. The HTV exhibits negative vorticity as the horizontal tail plane needs to be adjusted for negative lift due to trimmed flight. The negative circulation gradient in the wing-fuselage region leads to the counter-rotating WFV. The vortex sheet emanating from the wing trailing edge can clearly be observed and so can the vortex sheet shed at the horizontal tail plane. The two strongest vortices based on peak vorticity levels are the ONV and the OFV with the latter clearly being the strongest of all such distinct vortices. The maximum peak vorticity level of the OFV is associated with the highly loaded outboard flap. The relatively high vorticity level of the ONV is caused by the inclined ring profile of the nacelle subject to the crossflow caused by the swept wing. The "*s*-like" shape of the vortex sheet in that region indicates that the two vortices have rotated around each other by approximately 180 deg. Also, several less pronounced vortices indicated by smaller vorticity levels are present in between the six dominating wing vortices. These smaller vortices are caused by flow separations at slat horns, flap track fairings, and other geometric discontinuities of the wing. Local turbulence maxima are found in the regions of high velocity gradients, especially for the area of retarded axial core flow of the dominating vortices, Fig. 3b. These turbulence maxima are evoked

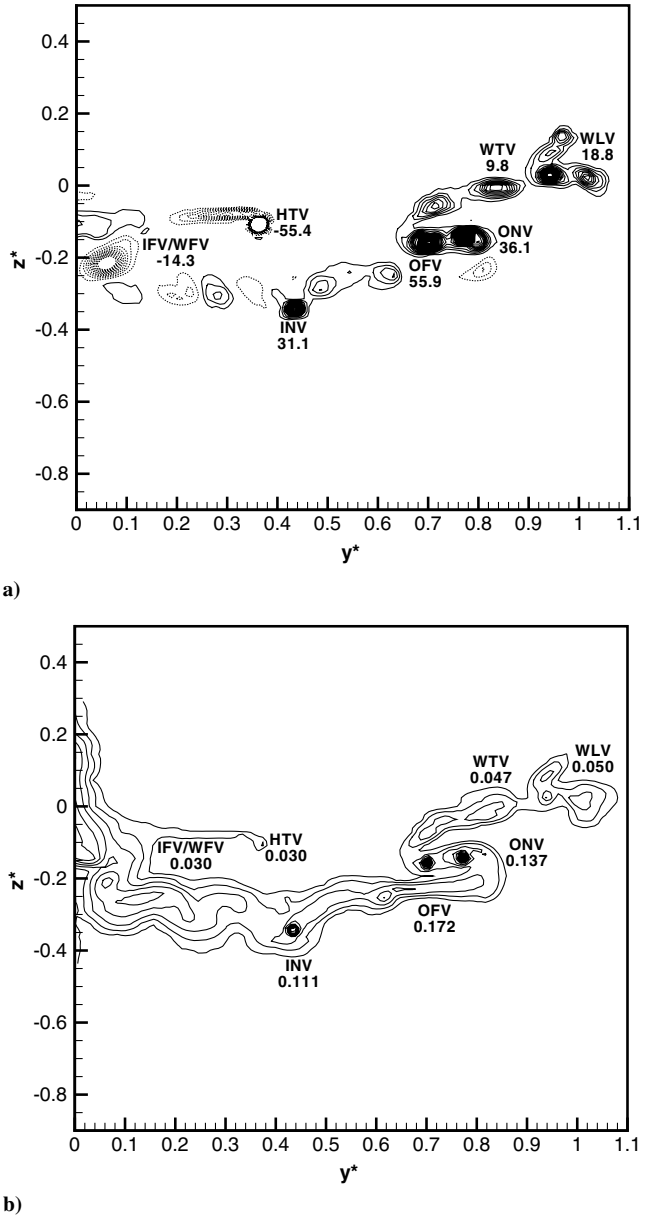

Fig. 3 Contour plots of nondimensional axial vorticity (ξ) and turbulence intensity (Tu_z) distributions at $x^* = 0.37$; $Re_{\bar{c}} = 0.5 \times 10^6$; a) ξ; solid lines: positive values, dashed lines: negative values; $-10 \leq \xi \leq 50$; $\triangle\xi = 1$; b) Tu_z; $0.02 \leq Tu_z \leq 0.2$; $\triangle Tu_z = 0.01$.

by the strong velocity gradient and streamline curvature in the vortex crossflow areas and by the inflection in the radial profiles of the retarded axial core flow. The fuselage wake is visible by a large region of increased turbulence intensity close to the plane of symmetry ($y^* = \approx 0, -0.4 < z^* < 0.3$). This region is larger than the fuselage diameter due to the upwash of the inclined fuselage and the downwash of the wing, which moves the fuselage turbulence wake from its original position resulting in a vertical stretching of the fuselage turbulence sheet.

Progressing downstream to $x^* = 5.6$, $\tau^* = 0.164$, three vortices remain at this station of the extended near field, Fig. 4. The strongest one is formed by the merging of the OFV with the ONV and WTV, which is then called the main vortex (MV), and the second one being the WLV. The third vortex is the HTV, which is also still visible, but its peak vorticity level is strongly reduced. Because of the induced velocity fields of the OFV/ONV and the WTV/WLV on the HTV, the latter sinks faster than the other two vortices. The IFV/WFV and the INV have fed vorticity to other vortical structures. In comparison to Fig. 3, the WLV has rotated around the merged OFV/ONV/WTV by

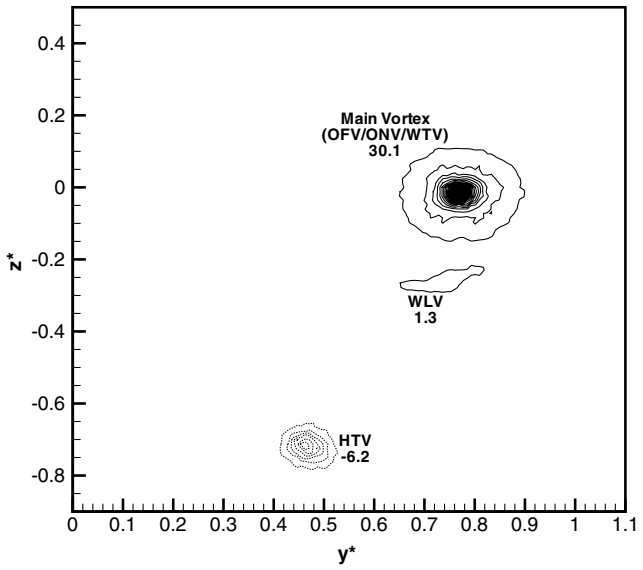

a)

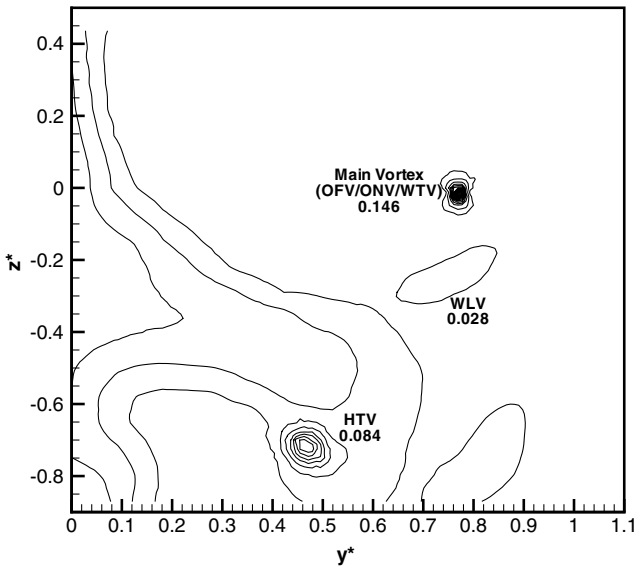

b)

Fig. 4 Contour plots of nondimensional axial vorticity (ξ) and turbulence intensity (Tu_z) distributions at $x^* = 5.6$; $Re_{\bar{c}} = 0.5 \times 10^6$; a) ξ; solid lines: positive values, dashed lines: negative values; $-10 \le \xi \le 50$; $\triangle\xi = 1$; b) Tu_z; $0.02 \le Tu_z \le 0.2$; $\triangle Tu_z = 0.01$.

approximately 230 deg with the peak vorticities clearly decreasing. Again, increased turbulence levels are attributed to the positions of the main vortices, Fig. 4b. The two strongest vortices are not influenced by the enlarged region of the fuselage wake, whereas the HTV is now fully embedded in this area.

Figure 5 illustrates the movement of the vortices for the y^*–z^* plane between $x^* = 0.02$, $\tau^* = 0.0006$ and $x^* = 5.6$, $\tau^* = 0.164$. The paths of four vortices are illustrated, namely, the HTV, INV, WLV, and ONV, which later becomes part of the main vortex. As the measuring plane at $x^* = 0.02$ is upstream of the horizontal tail plane, there is no data for the HTV at this station. There is also no data point available for the INV at $x^* = 5.6$ because the INV has dissipated. The WTV merges with OFV and ONV just before $x^* = 1.0$, $\tau^* = 0.029$, but for clarity they are not illustrated here. These three vortices form the main vortex, which exhibits the highest peak vorticity in the flowfield downstream of $x^* = 1.0$. The vortices rotate counterclockwise around the roll-up center ($y^* \approx 0.78$) which is located close to the position of the main vortex.

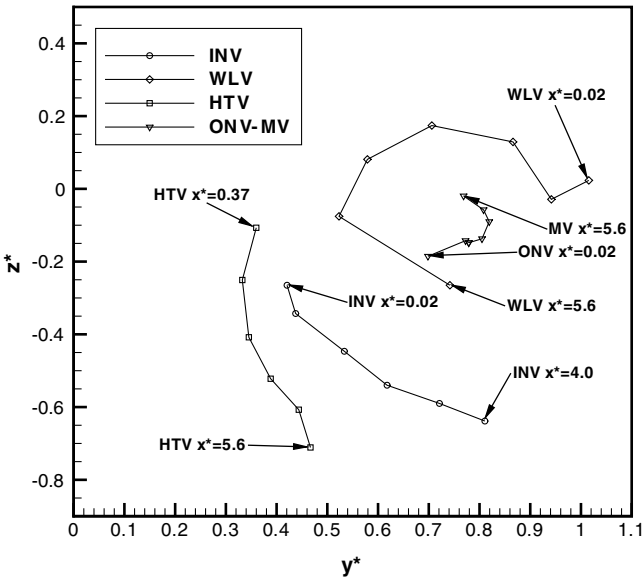

Fig. 5 Positions of the vortices between $x^* = 0.02$ and $x^* = 5.6$; $Re_{\bar{c}} = 0.5 \times 10^6$.

Further results concerning the influence of large winglet and static winglet flap deflection on the wake vortex development are documented in [32].

Oscillating Winglet Flaps

Measurements have been performed with both symmetrically and asymmetrically oscillating winglet flaps with maximum deflection angle of $\delta = 20$ deg for the frequency range of 1–40 Hz corresponding to $k_{\text{osc}} = 0.05$–1.987. Based on freestream velocity and wing semispan the reduced frequency $k = fb/(2U_\infty)$ serves as a nondimensional frequency parameter. The reduced frequency is also used as a similarity parameter to transfer values between small-scale and full-scale conditions. The frequency range of $k_{\text{osc}} \approx 0.05$–$2$ is chosen to cover the frequencies of dominant wake instabilities, namely, those of the Crow [34] and Crouch [35] type. Related reduced frequencies are $k_{\text{Crow}} = 0.08$–0.1 (long wave) and $k_{\text{Crouch}} = 0.12$–0.6 (long to medium wave), [36]. Details on the reduced frequency values are presented in the section on "Spectral Analysis."

The maximum flap deflection angle, $\delta = 20$ deg, is chosen for two reasons. On the one hand, the magnitude of the flap induced velocities at a certain frequency has to be large enough to amplify the initial disturbance level in the rolled-up vortex accelerating the development of long to medium wave instabilities responsible for wake vortex decay. On the other hand, the maximum deflection angles at full-scale frequencies are limited by the performance of real aircraft actuator systems. Here, the velocities induced by the oscillating winglet flaps are on the order of 25% with respect to the freestream velocity. They are aimed to increase the axial, lateral, and vertical velocity fluctuations at the frequencies of long wave instabilities in the rolled-up (main) vortex by at least a factor of 3 to 5. Therefore, mainly the crossflow plane at $x^* = 5.6$ is inspected and results are compared with those obtained without flap oscillations (baseline).

Force measurements are conducted with a maximum static flap deflection of $\delta = 20$ deg. A slight decrease in lift can be observed for both symmetrical (-1.7%) and asymmetrical (-0.6%) winglet flap deflections. The increase in the drag coefficient is about 2.1% for symmetrical winglet flap deflections and approximately 1.2% for asymmetrical deflections. Any change of the overall forces and moments is an important issue as the horizontal tail plane cannot be moved at such high frequencies as the winglet flaps, in order to keep the aircraft in a steady flight condition. The pitching moment coefficient stays almost constant at asymmetric deflections of lower and upper flaps, that is, flaps are deflected opposite at the same

nominal deflection angle, indicating a stable, straight, and level flight condition.

Wake Flowfield

The axial vorticity field at station $x^* = 5.6$ is evaluated for four cases, namely, two symmetrical and two asymmetrical oscillations at two frequencies, $f_{\mathrm{osc},1} = 4$ Hz, $k_{\mathrm{osc},1} = 0.199$ and $f_{\mathrm{osc},2} = 12$ Hz, $k_{\mathrm{osc},2} = 0.596$, Fig. 6. The results for these two frequency values are selected because they are related to the Crow-type instability for the (rolled-up) main vortex system ($k_{\mathrm{Crow}} \approx 0.08$–$0.1$, $k_{\mathrm{osc},1} \approx 2k_{\mathrm{Crow}}$) and the Crouch-type instability for the vortex system consisting of the neighboring corotating winglet vortex and main vortex ($k_{\mathrm{Crouch}} \approx 0.12$–$0.6$).

The vorticity fields indicate that the peak vorticity level attributed to the main vortex (merged OFV/ONV/WTV) is increased compared to the baseline case, compare Figs. 4 and 6. This raise in peak vorticity is between 5 and 32%. The WLV, which was still visible for the baseline configuration, has disappeared in the case of the lower oscillation frequency ($k_{\mathrm{osc}} = 0.199$, Figs. 6a and 6c. Here, the WLV has nearly completely merged with the main vortex leading to an increased peak vorticity level. In contrast, the WLV can still be detected at the higher oscillation frequency ($k_{\mathrm{osc}} = 0.596$, Figs. 6b and 6d). The peak vorticity level is of the same magnitude as for the baseline case (Fig. 4), but the WLV has progressed further in its counterclockwise rotation with respect to the baseline. The vorticity sheet connecting the WLV and the main vortex indicates the advanced merging of the two vortices. The shape and size of the main vortex does not differ markedly from the baseline configuration neither in vorticity nor in turbulence intensity distribution, Fig. 7. The presence of the WLV in case of the higher oscillation frequency can also be seen in the turbulence intensity pattern by an elliptic region of moderate turbulence intensity. Compared to the baseline case, increased turbulence levels between 17 and 20% are found for the main vortex core, except for the asymmetrical case at $k_{\mathrm{osc}} = 0.596$.

Figure 8 summarizes the downstream development of nondimensional axial peak vorticity $\xi_{\max}$, vortex core radius r_c/b, axial velocity deficit $(U_\infty - \bar{u}_{\min})/U_\infty$, and peak turbulence intensities $Tu_{x,y,z_{\max}}$ for the main vortex as a function of nondimensional

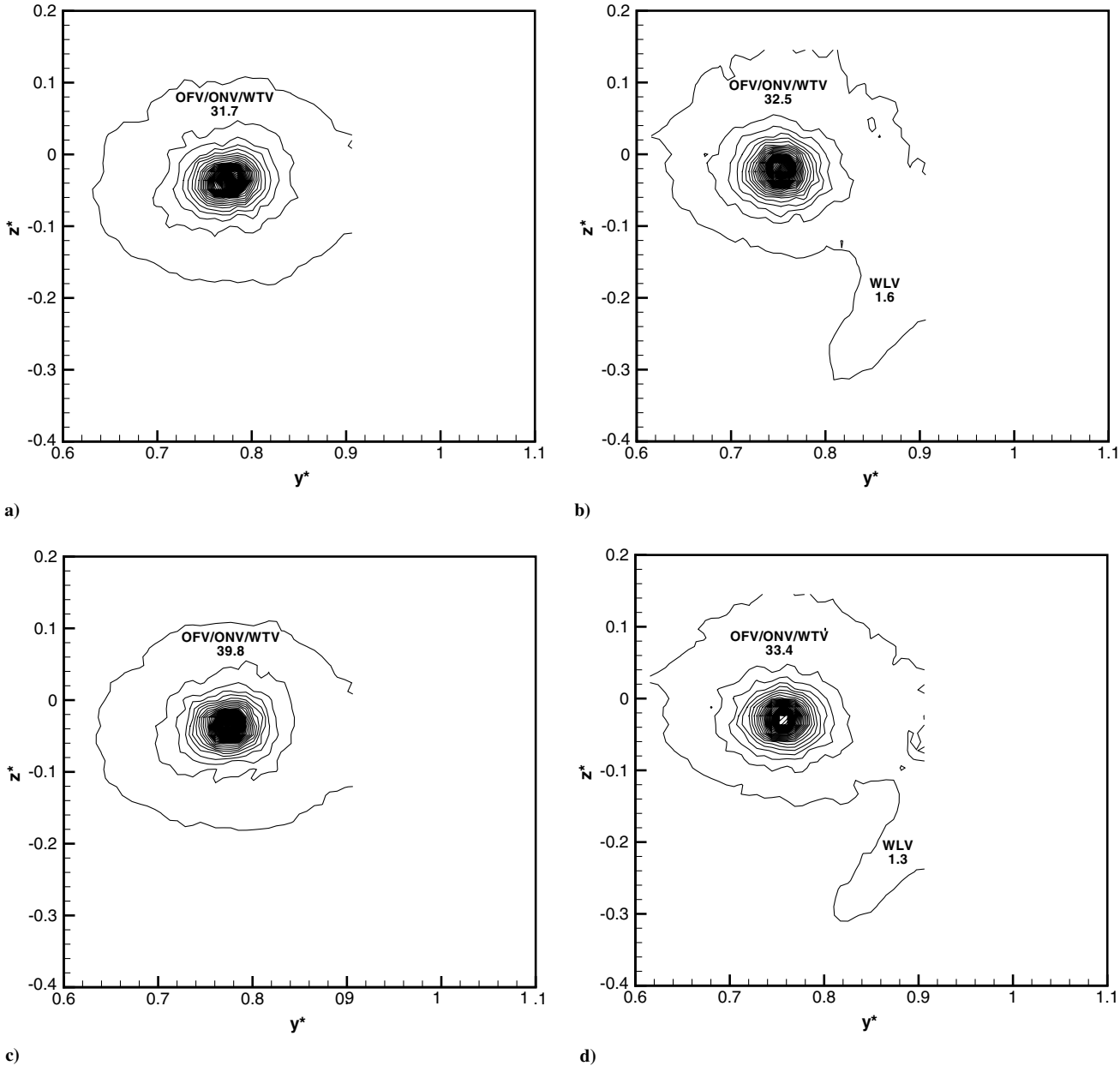

Fig. 6 Contour plots of nondimensional axial vorticity (ξ) distributions at $x^* = 5.6$; $Re_{\bar{c}} = 0.5 \times 10^6$; $1 \le \xi \le 50$; $\triangle\xi = 1$; a) symmetrical oscillation at $k = 0.199$; b) symmetrical oscillation at $k = 0.596$; c) asymmetrical oscillation at $k = 0.199$; d) asymmetrical oscillation at $k = 0.596$.

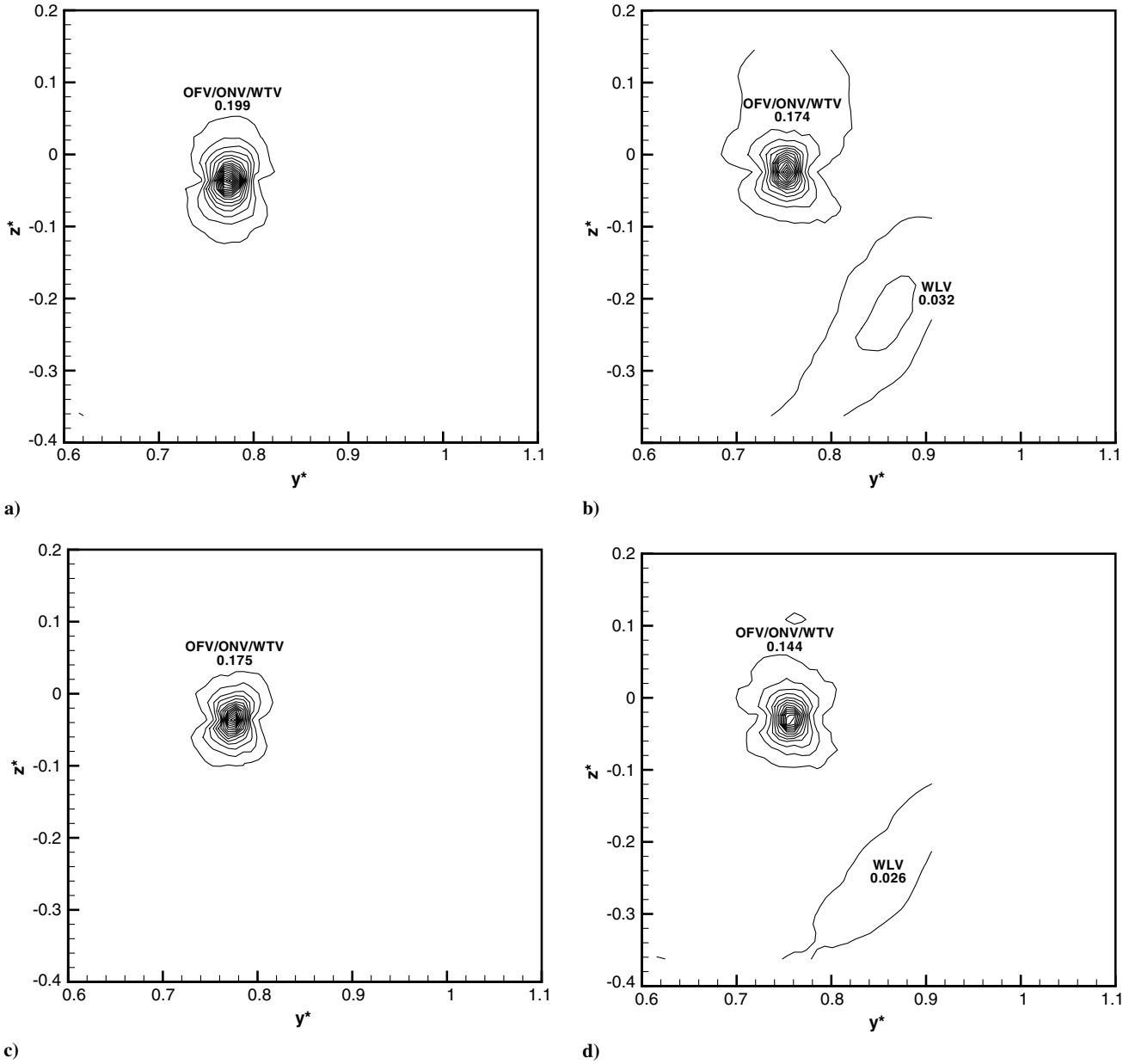

Fig. 7 Contour plots of turbulence intensity (Tu_z) distributions at $x^* = 5.6$; $Re_{\bar{c}} = 0.5 \times 10^6$; $0.02 \leq Tu_z \leq 0.2$; $\triangle Tu_z = 0.01$; a) symmetrical oscillation at $k = 0.199$; b) symmetrical oscillation at $k = 0.596$; c) asymmetrical oscillation at $k = 0.199$; d) asymmetrical oscillation at $k = 0.596$.

distance x^* and time τ^*. Data corresponding to static flap deflections are given in [32]. All results are obtained on measuring grids with identical spatial resolution. Figure 8a illustrates the decay in peak vorticity for the main vortex and the HTV due to turbulent diffusion ($d\xi/d\tau^*|_{MV} \cong 167$). The decay rate of the HTV is clearly higher, as the decay process is mainly influenced by the interaction with the highly turbulent fuselage wake. The peak vorticity levels for all vortices except the main vortex decrease downstream. Vorticity from other vortices, mainly the ONF and WTV, is fed during merging into the main vortex keeping its peak vorticity on a high level. The core radius is defined as the distance from the vortex center with zero crossflow velocity to the radial point of maximum crossflow velocity. The vortex core size shows a significant increase upstream of $x^* = 3.0$ followed by a drop progressing downstream. The strong increase in vortex core size is associated with the turbulent merging of dominant vortices (ONF and WTV) [37]. After roll up of the vorticity sheets the vortex core radius may decrease to some extent. At $x^* \approx 3.0$, the merging of the WLV with the main vortex starts. The axial velocity deficit shown in Fig. 8c illustrates a decreasing deficit up to $x^* = 4.0$, and thereafter the deficit increases to approximately 11%. This axial velocity deficit is a characteristic feature of the trailing vortices reflecting the retarded axial velocity due to the wing boundary layers and local trailing-edge flow separation. Figure 8d presents the peak turbulence intensities of all three velocity components. At $x^* = 5.6$ such peak turbulence intensities reach levels between 5 and 15%.

The results for the cases with winglet flap oscillations taken at station $x^* = 5.6$ are included in Fig. 8 and listed in Table 1. The values for static flap deflections are also presented in Table 1. Winglet flap oscillations lead to an increase in peak vorticity relative to the baseline case. Higher peak vorticity levels result from static flap deflections because additional "stationary" single vortices are created enhancing the merging process. Compared to the baseline case, the vortex core radius decreases stronger for oscillating flaps than for static flap deflections, reflecting again the accelerated roll-up process. A significant difference is shown for the axial velocity deficit for which static flap deflections exhibit higher values with respect to the baseline case whereas reduced values are found for the case of oscillating flaps, the latter due to enhanced turbulent mixing. The peak axial turbulence intensity of the vortex core area stays

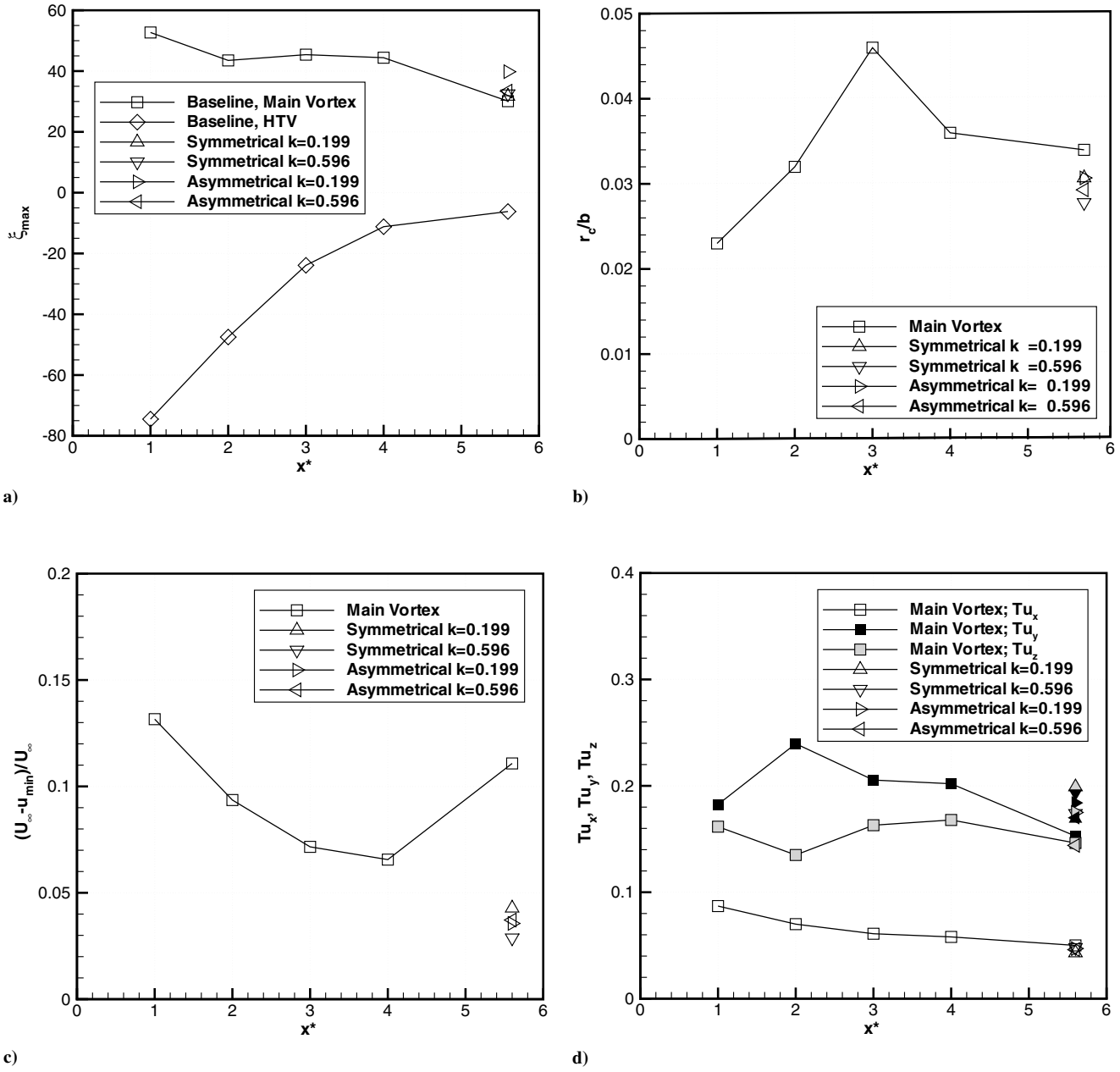

Fig. 8 Development of flowfield variables between $x^* = 1.0$ and $x^* = 5.6$; $Re_{\bar{c}} = 0.5 \times 10^6$; a) ξ_{max} for the main vortex and the HTV; b) r_c/b for the main vortex; c) $U_\infty - \bar{u}_{min}/U_\infty$ for the main vortex; d) $Tu_{x,max}$, $Tu_{y,max}$, and $Tu_{z,max}$ for the main vortex.

almost constant, whereas the lateral and vertical turbulence intensities increase in their levels markedly. An increase in lateral and vertical turbulence intensity is also present for static flap deflections, but the rms values are generally not as high as for the case of oscillating flaps. The data substantiate the fact that the oscillations of the winglet flaps can enhance vortex merging and lead to higher rms levels in velocity perturbations at the core of the remaining rolled-up vortex.

Table 1 Flow variables for core region of main vortex at $x^* = 5.6$

Case name	ξ_{max}	r_c/b	$(U_\infty - u_{min})/U_\infty$	Tu_x	Tu_y	Tu_z
Baseline	30.1	0.034	0.111	0.050	0.153	0.146
Static flap deflections [32]						
Symmetrical inboard	47.3	0.024	0.114	0.044	0.179	0.153
Symmetrical outboard	42.4	0.028	0.126	0.044	0.165	0.150
Asymmetrical inboard	46.4	0.025	0.126	0.044	0.135	0.150
Asymmetrical outboard	44.0	0.025	0.157	0.042	0.144	0.147
Oscillating flaps						
Symmetrical $k = 0.199$	31.7	0.031	0.043	0.043	0.169	0.199
Symmetrical $k = 0.596$	32.5	0.028	0.029	0.048	0.193	0.174
Asymmetrical $k = 0.199$	39.8	0.031	0.036	0.047	0.184	0.175
Asymmetrical $k = 0.596$	33.4	0.029	0.037	0.046	0.170	0.144

Spectral Analysis

Power spectral densities are analyzed to detect peaks associated with the velocity perturbations introduced into the vortex wake by the oscillating winglet flaps. They are aimed to enhance the development of inherent wake instability mechanisms. Spectral densities $S^N_{u'}$ of the axial velocity fluctuations u' are evaluated for the core region of the WLV at $x^* = 0.02$ and $x^* = 0.37$ and also for the core region of the main vortex at $x^* = 5.6$. The calculation uses fast Fourier transformation and linear band averaging with $n_B = 1024$ frequency bands. The spectral values are normalized with the variance of the velocity fluctuations $\overline{u'^2}$ and the frequency interval of band averaging $\Delta f = f_M/(2n_B) = \Delta k U_\infty/(b/2)$, therefore multiplied by $(\Delta k U_\infty)/(\overline{u'^2}(b/2))$. These nondimensional spectral densities are plotted as a function of reduced frequency k and presented for both symmetrical and asymmetrical oscillations of the winglet flaps.

Considering the WLV core at the most upstream station ($x^* = 0.02$), distinct spectral peaks can be detected at reduced frequencies corresponding to the winglet flap oscillation frequencies and at reduced frequencies associated with the higher harmonics, Fig. 9. The symmetrically, that is, in-phase, deflected flaps produce larger spectral peaks than the asymmetrically deflected flaps with 180 deg phase shift. In that case, the lower and upper winglet flaps are deflected in opposite directions creating additional side edge vortices so that turbulent mixing diminishes the spectral values related to the oscillation frequencies. Moving downstream to the WLV core at station $x^* = 0.37$, Fig. 10 reveals even increased values of the well-defined spectral peaks caused by flap oscillations. The spectral peaks of the symmetrical case show values up to 18.8, which are again higher compared to the asymmetrical case with peak values of 5.4. Concentrating on the main vortex core at station $x^* = 5.6$, the spectra of the symmetrical case exhibit significant energy overshoots at the frequencies of the winglet flap oscillations for all five considered reduced frequencies, Fig. 11. For the asymmetrical case, smaller spectral peaks are observed increasing in amplitude with increasing oscillation frequency. Overall, the velocity fluctuations ingested at $x^* = 0.0$ by the oscillating winglet flaps into the vortices at the wing tip are still present in the rolled-up vortex at $x^* = 5.6$. The relative levels of these frequency dependent velocities are in the range of 10% with respect to the freestream velocity.

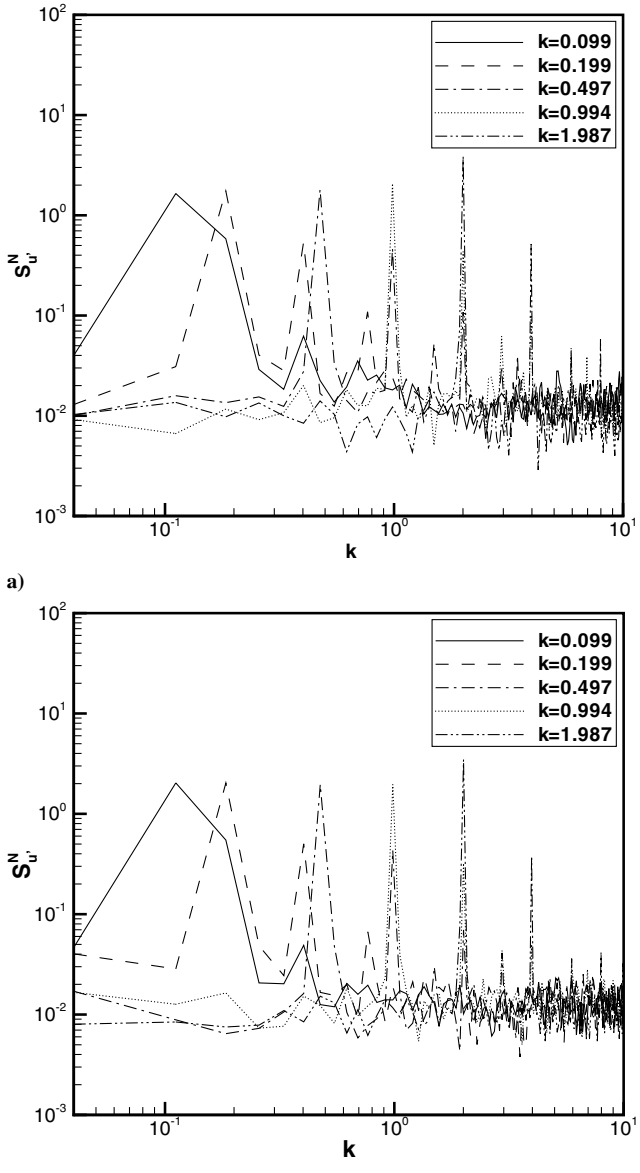

Fig. 9 Normalized power spectral densities of the axial velocity fluctuations at $x^* = 0.02$; $Re_{\bar{c}} = 0.5 \times 10^6$; a) symmetrical oscillations; b) asymmetrical oscillations.

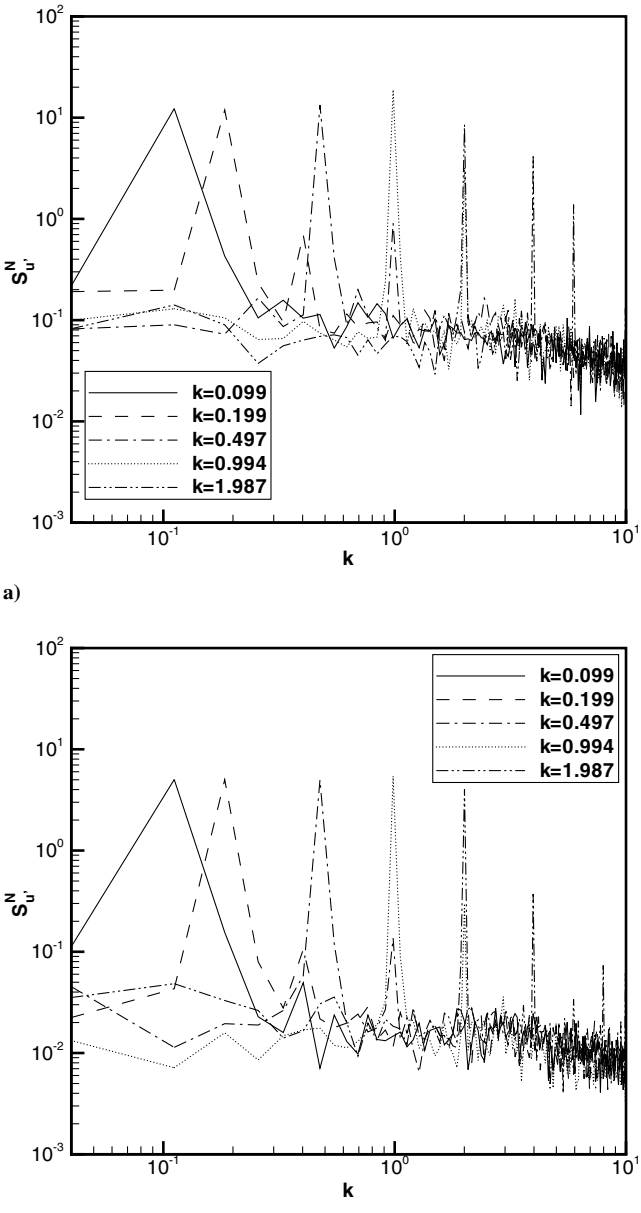

Fig. 10 Normalized power spectral densities of the axial velocity fluctuations at $x^* = 0.37$; $Re_{\bar{c}} = 0.5 \times 10^6$; a) symmetrical oscillations; b) asymmetrical oscillations.

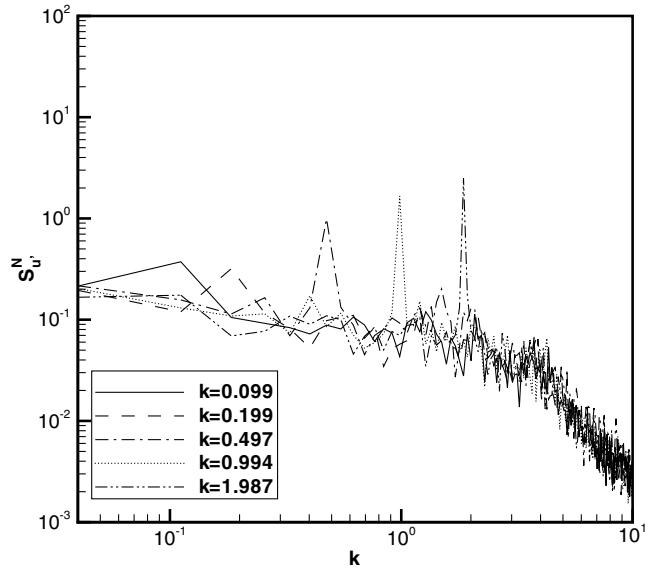

a)

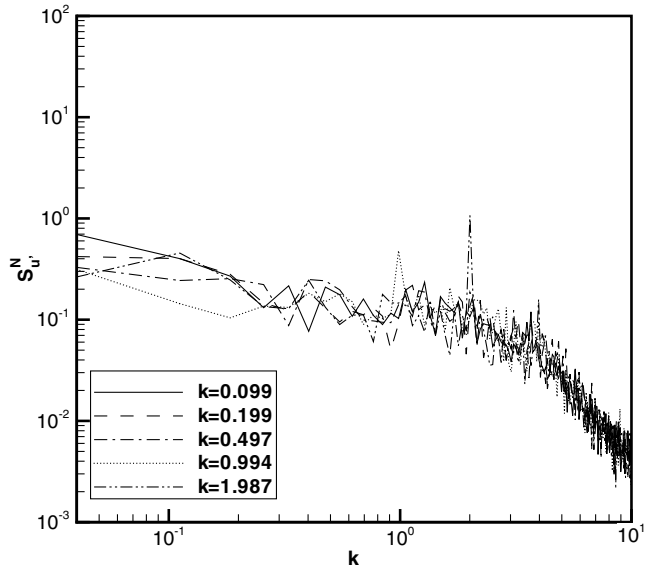

b)

Fig. 11 Normalized power spectral densities of the axial velocity fluctuations at $x^* = 5.6$; $Re_{\bar{c}} = 0.5 \times 10^6$; a) symmetrical oscillations; b) asymmetrical oscillations.

A spectral investigation for a complete frequency band of winglet flap oscillations is conducted for the rolled-up (main) vortex at station $x^* = 5.6$. The relative difference between the spectra for the cases of oscillating winglet flaps and baseline configuration is analyzed for axial, lateral, and vertical velocity fluctuations. Considering, for example, the axial velocity fluctuations this difference is given by $(S^N_{u'_{\text{osc}}}(k) - S^N_{u'_{\text{baseline}}}(k))/S^N_{u'_{\text{baseline}}}(k)$. The relationship corresponds to discrete Fourier transformation of ergodic time series with same sampling frequency and sampling interval [38]. Results are plotted in Figs. 12 and 13 as a function of the reduced frequency k and the reduced oscillation frequency k_{osc}. Figure 12 refers to the case of symmetrical flap oscillations, Fig. 13 to the asymmetrical case. As proven in Fig. 11, the spectral peaks associated with the oscillation frequency k_{osc} are mostly much larger than the corresponding values of the baseline configuration (oscillation off). Consequently, the relative difference between these values results in local maxima along a diagonal line, indicated by values beyond 2. This diagonal trace reflects a synchronous forcing of desired disturbances by introducing frequency dependent velocity fluctuations. In addition, vertical traces of peaks in the spectral differences are detected, for example, at reduced frequencies of

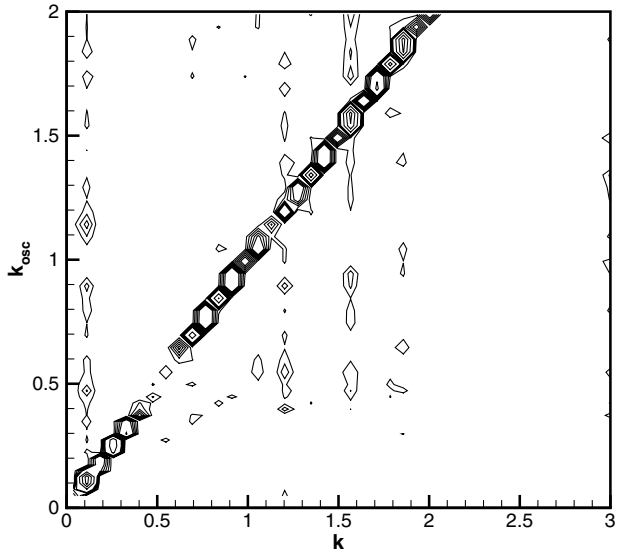

a)

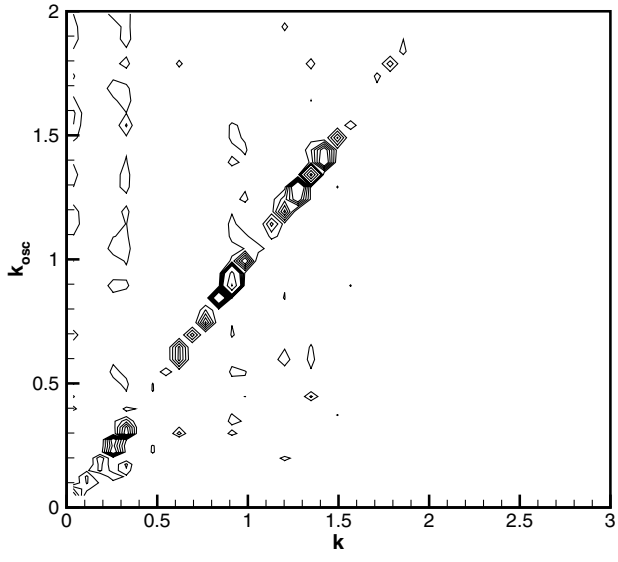

b)

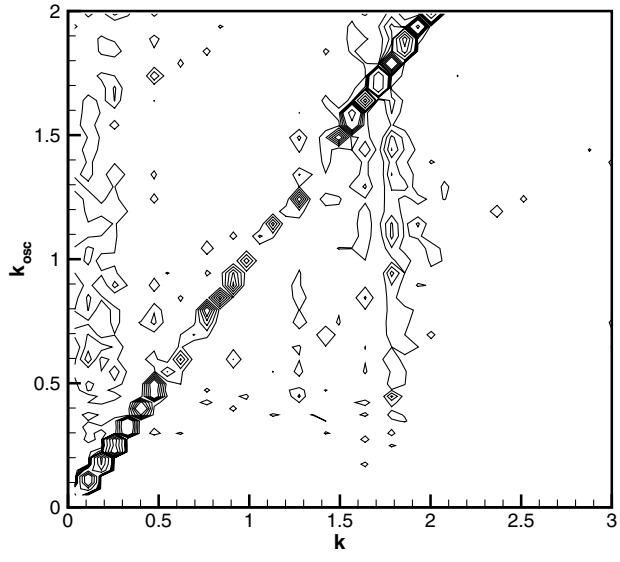

c)

Fig. 12 Relative difference of the power spectral densities for different frequencies of symmetrical flap oscillations with reference to the baseline configuration at $x^* = 5.6$; $Re_{\bar{c}} = 0.5 \times 10^6$; isolines plotted for 1, 2, 3, 4, 5, 10, 15, 20; a) $\triangle S_{u'}$; b) $\triangle S_{v'}$; c) $\triangle S_{w'}$.

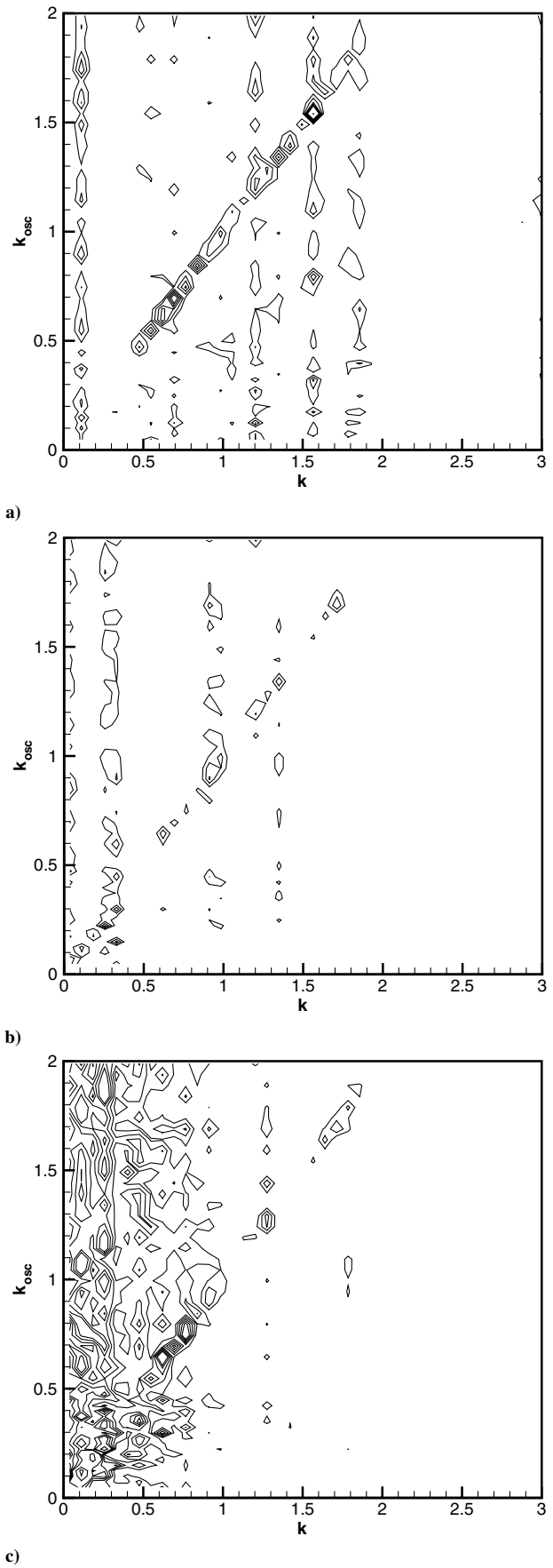

Fig. 13 Relative difference of the power spectral densities for different frequencies of asymmetrical flap oscillations with reference to the baseline configuration at $x^* = 5.6$; $Re_{\tilde{c}} = 0.5 \times 10^6$; isolines plotted for 1, 2, 3, 4, 5, 10, 15, 20; a) $\triangle S_{u'}$; b) $\triangle S_{v'}$; c) $\triangle S_{w'}$.

$k \approx 0.1$ and $k \approx 0.3$, reflecting also narrowband concentrations of turbulent kinetic energy. These peaks along vertical lines indicate an increase of the velocity fluctuations at specific frequencies independent of the specific forcing frequency, that is, the effect of a receptive mechanism to asynchronous forcing.

The presence of instability mechanisms propagating along the vortex wake in streamwise direction can lead to a relevant distortion of the trailing vortex pair, accelerating its decay and dispersion. Typically, long and short wave instabilities occur. The dominant long wave instability of a vortex pair is the Crow instability [34]. This instability is related to the strain effect induced by one vortex of a pair on the other one, and appears as a sinusoidal displacement of the vortex trajectories ultimately responsible for the wake vortex collapse in the far field. The trajectory displacement grows exponentially with time until the counter-rotating vortices link at points of minimum lateral distance. Thus, the vortex system becomes disorganized leading to rapid wake vortex decay. The wavelength of the Crow-type instability is approximately $\lambda_{\text{Crow}} \approx 8b_0$ based on linear stability theory [34]. The quantity b_0 is the distance of the vortex pair, with $b_0 = 0.76b$–$0.78b$ for the present case, compare Figs. 4 and 7. This wavelength corresponds to a reduced frequency of $k_{\text{Crow}} = f_{\text{Crow}}(b/2)/U_\infty = b/(2\lambda_{\text{Crow}}) \approx 0.08$. Velocity fluctuations caused by turbulence or fed actively into the vortex wake represent inhomogeneous forcing terms with respect to stability theory. The influence of turbulence on wake vortex life spans was investigated, for example, by Crow and Bate [24]. Regarding linear stability theory the velocity perturbation at the core of the trailing vortex is then composed by the component due to mutual induction and the component related to superimposed fluctuations. Introducing such fluctuations at the frequency of the inherent instability may significantly reduce the time for vortex linking. Rapid wake decay will then start within a shorter trailing distance compared to the nonperturbed case. Further, Figs. 12 and 13 show a vertical line of local spectral maxima at a reduced frequency of $k \approx 0.1$ which is close to the value of k_{Crow}. It indicates that the development of the Crow-type instability is also accelerated to a certain extent by asynchronous forcing.

The vorticity pattern shows that for some cases two vortex pairs are still present at $x^* = 5.6$ consisting of the weak winglet vortex (WLV) and the main vortex (merged OFV/ONV/WTV), compare Figs. 6 and 7. Further instabilities are related to the case of two vortex pairs with corotating neighbored vortices. The instability and transient growth of such vortex systems was analyzed by Crouch [35]. The instabilities are periodic along the axes of the vortices. They include a symmetrical mode corresponding to the long wave Crow instability, but also additional symmetric and asymmetric modes are present. The wavelengths of the latter are shorter than those of the Crow instability, but large with respect to the effective vortex core size. The growth rate can be twice that of the Crow instability and transient growth of the long wave instability can amplify an initial disturbance by a factor of 10. For the Crouch instability the wavelength is given by $\lambda_{\text{Crouch}} \approx 1.5\tilde{b}_0$–$6.0\tilde{b}_0$, $\tilde{b}_0 = 0.55b$–$0.8b$. This leads to a reduced frequency range of $k_{\text{Crouch}} \approx 0.12$–$0.6$ [36]. The vertical line of the local spectral maxima at $k \approx 0.3$, observed in Figs. 12 and 13 for the lateral velocity fluctuations, falls within this frequency range. It indicates that the development of such instabilities can also be provoked by introducing controlled disturbances.

In summary, the oscillation of the winglet flaps leads to a concentration of turbulent kinetic energy in the frequency range of dominant inherent instabilities for both, symmetrical and asymmetrical, cases. Although the oscillations with asymmetrically deflected flaps show lower amplifications in comparison to the symmetrical case, it is still favorable as the oscillations in lift, side force, and pitching moment are far lower as for symmetric oscillations.

Two-Point Correlations

Correlation measurements with two hot-wire probes are also conducted. The first probe is positioned at station $x_1^* = 0.02$ and

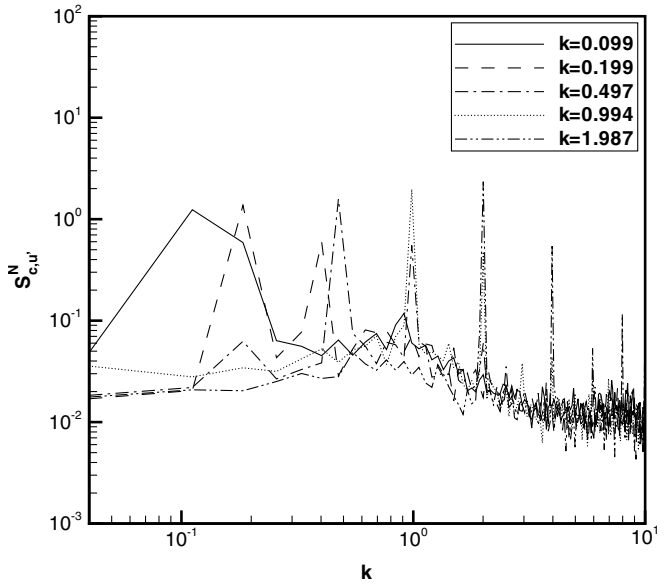

a)

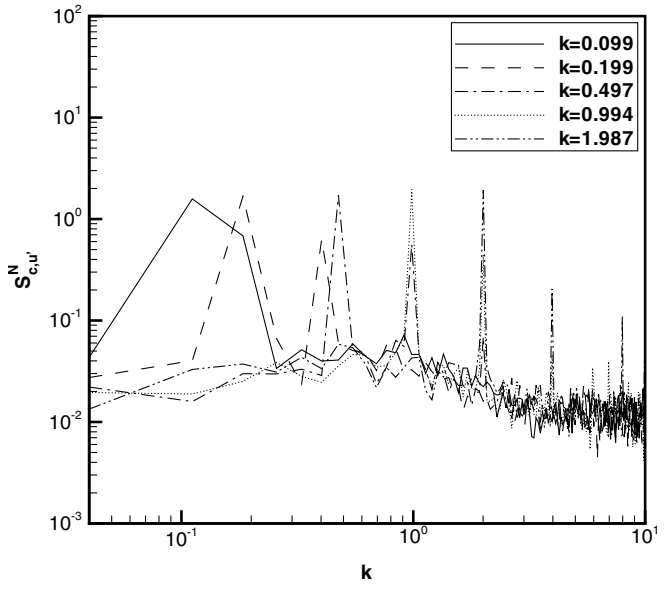

b)

Fig. 14 Normalized cross-spectral densities of the amplitude of the axial velocity fluctuations for stations $x_1^* = 0.02$ and $x_2^* = 5.6$; $Re_{\bar{c}} = 0.5 \times 10^6$; a) symmetrical oscillations; b) asymmetrical oscillations.

correlated with the second probe at station $x_2^* = 5.6$. The probes are positioned in the core region of the WLV ($x_1^* = 0.02$) and the main vortex ($x_2^* = 5.6$) at the same locations as taken for evaluation of the power spectral densities shown in Figs. 9 and 11.

Normalized cross spectral densities $S^N_{c,u'}$ of the axial velocity fluctuations u' are plotted against the reduced frequency k, Fig. 14. The calculation of the cross-spectral densities is performed using the same parameters as for the power spectral densities. Results are shown again for symmetrical and asymmetrical winglet flap oscillations. Distinct spectral peaks are clearly visible at reduced frequencies corresponding to the oscillation frequencies and their higher harmonics. The amplitudes of these peaks are comparably high for both types of oscillations indicating the dominance of the forced oscillations being convected from near-field to extended near-field positions. Figure 15 contains the phase angle distributions of the axial velocity fluctuations as a function of the reduced frequency for the asymmetrical oscillations. Phase angles at the values of the reduced oscillation frequencies are within a band of 180 ± 30 deg.

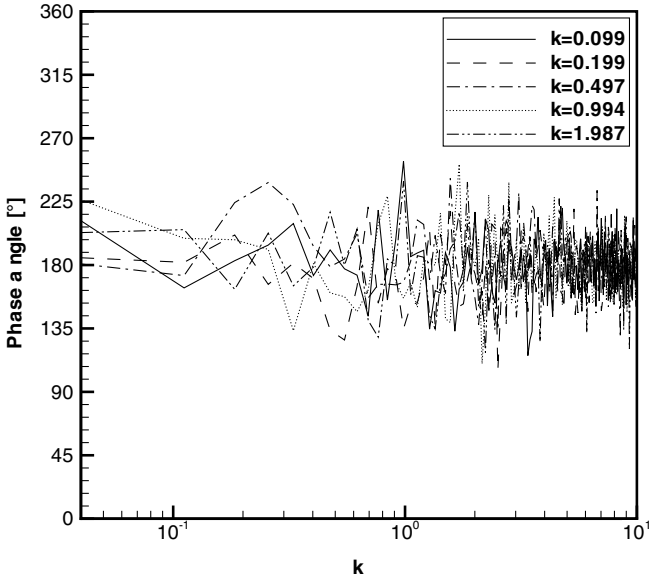

Fig. 15 Phase spectrum of cross-spectral densities of the axial velocity fluctuations for asymmetrical winglet flap oscillations for stations $x_1^* = 0.02$ and $x_2^* = 5.6$; $Re_{\bar{c}} = 0.5 \times 10^6$.

Conclusions

The wake vortex development of a large transport aircraft in approach configuration fitted with large winglet and oscillating winglet flaps is investigated by experimental means. A detailed four engined half-model of 1:32 scale is studied at an angle of attack of 6.5 deg and a Reynolds number based on the mean aerodynamic chord of 0.5×10^6. Vorticity and turbulence intensity as well as spectral density and cross-spectral density distributions are analyzed in the near and extended near field based on advanced hot-wire anemometry. The winglet flap oscillations are aimed to introduce desired perturbations in the wake flowfield to promote and amplify the development of inherent far-field wake instabilities. It is shown that the generated near-field disturbances (at $x^* = 0$) are still present at the farthest downstream plane (at $x^* = 5.6$). The oscillation frequencies are chosen to match the frequency range of the wake instabilities. The main results of this study can be summarized as follows:

1) The wake near field shows seven particular vortices, namely, from outboard to inboard, the WLV, the WTV, the OFV, the ONV and INV, the IFV/WFV, and the HTV. These vortices are connected through the vortex sheet shed at the wing trailing edge, except for the HTV. Positive axial vorticity is attributed to WLV, WTV, OFV, ONV, and INV, whereas IFV/WFV and HTV show negative axial vorticity. The latter is caused by the negative circulation gradient at the wing-fuselage junction and the negative lift of the horizontal tail plane needed for trimmed flight. The highest level of axial peak vorticity is given by the OFV because of the highly loaded outboard flap. It is located close to the free circulation centroid which is the wake vortex roll-up center.

2) In the extended near field the position and strength of the particular vortices change progressively because of the wake roll-up process and vortex merging. This process forms the remaining rolled-up vortex to which most of the vorticity is fed up to $\tau^* \approx 0.16$. The core regions of the particular wake vortices are characterized by axial vorticity peaks and considerable axial velocity deficits (8–11%). The vortex core structure exhibits maximum turbulence intensities on the order of 5–20%.

3) Spectral analysis of the velocity fluctuations shows a specific narrowband concentration of turbulent kinetic energy in the core of the rolled-up vortex, mainly at the frequencies of the winglet flap oscillations. The velocity spectra show peak values at these frequencies raising the perturbation level by a factor of 5 to 20 compared to the case of static flap deflection or oscillation off. This synchronous forcing can amplify the long wave Crow-type

instability in which the time is reduced when the process of vortex linking leading to rapid wake vortex decay starts.

4) Quasiperiodic fluctuations occur also for asynchronous forcing. Fluctuations are amplified at a reduced frequency of $k \approx 0.1$ corresponding to the frequency of the Crow-type instability. In addition, increased amplitudes are present at $k \approx 0.3$ which is in the range of reduced frequencies for the Crouch-type instability. This instability is related to the mutual induction of two vortex pairs with corotating neighbored vortices which is here the main trailing vortex interacting with the weak winglet vortex. This interaction leads to the amplification of the involved instabilities also contributing to wake vortex collapse.

As these investigations are limited to the range of the extended near field, further experiments are planned to prove the expected enhanced wake vortex decay in the far field. The focus is on a towing tank test using an existing detailed large transport aircraft model, thus increasing the wake distance up to about 80 wing spans. In addition, the measured disturbance velocities are used as start conditions for stability analysis simulations.

Acknowledgment

The support of this investigation within the framework of "IHK—Innovative High-Lift Configurations" by the German Government, Federal Ministry of Economics and Technology, under contract number 20A0301J is gratefully acknowledged.

References

[1] Hünecke, K., "Structure of a Transport Aircraft-Type Near Field Wake," *The Characterisation & Modification of Wakes from Lifting Vehicles in Fluids*, CP-584, AGARD, May 1996, pp. 5-1–5-9.

[2] Brenner, F., "Air Traffic Control Procedures for the Avoidance of Wake Vortex Encounters: Today and Future Developments by Deutsche Flugsicherung GmbH," *The Characterisation & Modification of Wakes from Lifting Vehicles in Fluids*, CP-584, AGARD, May 1996, pp. 4-1–4-14.

[3] Gerz, T., "Wake Vortex Prediction and Observation: Towards an Operational System," *Proceedings of ODAS 2001, S1-3*, ONERA-DLR Aerospace Symposium, ONERA, Chatillon, France, June 2001, ISBN 2-7257-006-X.

[4] Betz, A., "Das Verhalten von Wirbelsystemen," *Zeitschrift für Angewandte Mathematik und Mechanik*, Vol. 12, No. 3, 1932, pp. 164–174.
doi:10.1002/zamm.19320120307

[5] Donaldson, C. P., and Bilanin, A. J., "Vortex Wakes of Conventional Aircraft," AGARDograph, No. 204, May 1975.

[6] Devenport, W. J., Rife, M. C., Liapis, S. I., and Follin, G. J., "The Structure and Development of a Wing-Tip Vortex," *Journal of Fluid Mechanics*, Vol. 312, 1996, pp. 67–106.
doi:10.1017/S0022112096001929

[7] Spalart, P. R., "Airplane Trailing Vortices," *Annual Review of Fluid Mechanics*, Vol. 30, 1998, pp. 107–138.
doi:10.1146/annurev.fluid.30.1.107

[8] Rossow, V. J., "Lift-Generated Vortex Wakes of Subsonic Transport Aircraft," *Progress in Aerospace Sciences*, Vol. 35, No. 6, 1999, pp. 507–560.
doi:10.1016/S0376-0421(99)00006-8

[9] Hünecke, K., "From Formation to Decay—Extended-Time Wake Vortex Characteristics of Transport-Type Aircraft," AIAA Paper 2002-3265, June 2002.

[10] Henke, R., "Validation of Wing Technologies on an Airbus A340 Flying Testbed: First Flight Test Results from the European Program AWIATOR," International Council of the Aeronautical Sciences (ICAS) Paper 2004-4.4.1, Sept. 2004.

[11] Coustols, E., Stumpf, E., Jacquin, L., Moens, F., Vollmers, H., and Gerz, T., "Minimised Wake: A Collaborative Research Programme on Aircraft Wake Vortices," AIAA Paper 2003-0938, Jan. 2003.

[12] Gerz, T., Holzäpfel, F., and Darracq, D., "Commercial Aircraft Wake Vortices," *Progress in Aerospace Sciences*, Vol. 38, No. 3, 2002, pp. 181–208.
doi:10.1016/S0376-0421(02)00004-0

[13] Köpp, F., Rahm, S., Smalikho, I., Dolfi, A., Cariou, J.-P., Harris, M., and Young, R. I., "Comparison of Wake-Vortex Parameters Measured by Pulsed and Continuous-Wave Lidars," *Journal of Aircraft*, Vol. 42, No. 4, 2005, pp. 916–923.
doi:10.2514/1.8177

[14] Winckelmans, G. S., "Vortex Methods," *The Encyclopedia of Computational Mechanics*, edited by E. Stein, R. de Borst, and T. J. R. Hughes, Wiley, Vol. 3, 2004.

[15] Stumpf, E., "Study of Four-Vortex Aircraft Wakes and Layout of Corresponding Aircraft Configurations," *Journal of Aircraft*, Vol. 42, No. 3, 2005, pp. 722–730.
doi:10.2514/1.7806

[16] Holzäpfel, F., Hofbauer, T., Darracq, D., Moet, H., Garnier, F., and Gago, C. F., "Analysis of Wake Vortex Decay Mechanism in the Atmosphere," *Aerospace Science and Technology*, Vol. 7, No. 4, 2003, pp. 263–275.
doi:10.1016/S1270-9638(03)00026-9

[17] Breitsamter, C., Bellastrada, C., and Laschka, B., "Investigations on the Turbulent Wake Vortex Flow of Large Transport Aircraft," *ICAS Proceedings, 23rd International Congress of the Aeronautical Sciences*, ICAS, Sept. 2002, pp. 382.1–382.13.

[18] Elsenaar, A., "The Optimum Wing Load Distribution to Minimize Wake Hazard," *Conference on Capacity and Wake Vortices*, Imperial College, London, Sept. 2001.

[19] Breitsamter, C., "Beeinflussung des Nachlaufwirbelsystems von Großflugzeugen," *Proceedings DGLR-Symposium: The Airport as a Neighbour—Challenges and Solutions for future Air Transport Systems*, DGLR Rept. 2004-06, Oct. 2004.

[20] Jacquin, L., Fabre, D., Sipp, D., Theofilis, V., and Vollmers, H., "Instabilities and Unsteadiness of Aircraft Wake Vortices," *Aerospace Science and Technology*, Vol. 7, No. 8, 2003, pp. 577–593.
doi:10.1016/j.ast.2003.06.001

[21] Rennich, S. C., and Lele, S. K., "Method for Accelerating the Destruction of Aircraft Wake Vortices," *Journal of Aircraft*, Vol. 36, No. 2, 1999, pp. 398–404.
doi:10.2514/2.2444

[22] Durston, D. A., Walker, S. M., Driver, D. M., Smith, S. C., and Savas, Ö., "Wake Vortex Alleviation Flow Field Studies," *Journal of Aircraft*, Vol. 42, No. 4, 2005, pp. 894–907.
doi:10.2514/1.7904

[23] Fabre, D., and Jacquin, L., "Stability of a Four-Vortex Aircraft Wake Model," *Physics of Fluids*, Vol. 12, No. 10, 2000, pp. 2438–2443.
doi:10.1063/1.1289397

[24] Crow, S. C., and Bate, E. R., Jr., "Lifespan of Trailing Vortices in a Turbulent Atmosphere," *AIAA Journal*, Vol. 13, No. 7, 1976, pp. 476–482.

[25] Crouch, J. D., Miller, G. D., and Spalart, P. R., "Airplane Trailing Vortices," *Boeing Aero Magazine*, No. 14, 2001, pp. 1–8.

[26] Crouch, J. D., Miller, G. D., and Spalart, P. R., "Active-Control System for Breakup of Airplane Trailing Vortices," *AIAA Journal*, Vol. 39, No. 12, 2001, pp. 2374–2381.
doi:10.2514/2.1244

[27] Haverkamp, S., Neuwerth, G., and Jacob, D., "Active and Passive Vortex Wake Mitigation Using Control Surfaces," *Aerospace Science and Technology*, Vol. 9, No. 1, 2005, pp. 5–18.
doi:10.1016/j.ast.2004.08.005

[28] Kauertz, S., and Neuwerth, G., "Excitation of Instabilities in the Wake of an Airfoil with Winglets," *AIAA Journal*, Vol. 45, No. 3, 2007, pp. 577–598.
doi:10.2514/1.26462

[29] Voß, G., Stumpf, E., Konrath, E., v. Carmer, C., Krückeberg, C. P., and Meyer, H., "Wake Vortex Alleviation by Differential and Oscillating Flap Settings: A Numerical and Experimental Study," *The DLR Project Wake Vortex—Detecting, Characterizing, Controlling, Attenuating and Predicting Aircraft Wake Vortices*, Deutsches Zentrum für Luft- und Raumfahrt e.V., DLR Research Report 2008-15, 2008, pp. 1–26 (ISSN 1434-8454).

[30] Greenblatt, D., "Managing Flap Vortices via Separation Control," *AIAA Journal*, Vol. 44, No. 11, 2006, pp. 2755–2764.
doi:10.2514/1.19664

[31] Vey, S., Paschereit, O. C., Greenblatt, D., and Meyer, R., "Flap Vortex Management by Active Gurney Flaps," AIAA Paper 2008-286, Jan. 2008.

[32] Allen, A., and Breitsamter, C., "Transport Aircraft Wake Influenced by a Large Winglet and Winglet Flaps," *Journal of Aircraft*, Vol. 45, No. 2, 2008, pp. 686–699.
doi:10.2514/1.32787

[33] Breitsamter, C., "Turbulente Strömungsstrukturen an Flugzeugkonfigurationen mit Vorderkantenwirbeln," Ph.D. Thesis, DM 18432, Technische Universität München, Herbert Utz Verlag Wissenschaft (Aerodynamik), Germany (ISBN 3-89675-201-4), June 1997.

[34] Crow, S. C., "Stability Theory for a Pair of Trailing Vortices," *AIAA Journal*, Vol. 8, No. 12, 1970, pp. 2172–2179.
doi:10.2514/3.6083

[35] Crouch, J. D., "Instability and Transient Growth for Two Trailing-Vortex Pairs," *Journal of Fluid Mechanics*, Vol. 350, 1997, pp. 311–330.
doi:10.1017/S0022112097007040

[36] Breitsamter, C., "Nachlaufwirbelsysteme großer Transportflugzeuge–Experimentelle Charakterisierung und Beeinflussung. Habilitationsschrift," Technische Universität München, Herbert Utz Verlag (Aerodynamik), Germany (ISBN 3-8316-0713-3), Feb. 2007.

[37] Meunier, P., and Leweke, T., "Three-Dimensional Instability During Vortex Merging," *Physics of Fluids*, Vol. 13, No. 10, 2001, pp. 2747–2750.
doi:10.1063/1.1399033

[38] Marple, S. L., Jr., *Digital Spectral Analysis with Applications*, Prentice–Hall, Englewood Cliffs, NJ, 1987, pp. 25–56, 111–125, 386–394.